

Structure of Silica Xerogels Synthesized with Organoalkoxysilane Co-reactants Hints at Multiple Phase Separation

Cédric J. Gommès,^{*,†} Monika Basiura,[‡] Bart Goderis,[‡] Jean-Paul Pirard,[†] and Silvia Blacher[†]

Laboratoire de Génie Chimique, Département de Chimie Appliquée, Université de Liège, bâtiment B6a, Allée du 6 août 3, B-4000 Liège, Belgium, and Laboratorium voor Macromoleculaire Structuurchemie, Departement Scheikunde, Katholieke Universiteit Leuven, Celestijnenlaan 200F, B-3001 Heverlee, Belgium

Received: September 8, 2005; In Final Form: February 7, 2006

The microstructure of hybrid silica xerogels synthesized by the base-catalyzed polymerization of tetraethoxysilane (TEOS) in ethanol in the presence of 3-aminopropyltriethoxysilane (AES) and of 3-(2-aminoethylamino)propyltrimethoxysilane (EDAS) as co-reactants, and dried in subcritical conditions, is analyzed. A thorough structural characterization of the samples is performed combining nitrogen adsorption, small-angle X-ray scattering (SAXS), and transmission electron microscopy coupled with digital image analysis. The use of these methods shows that, for both co-reactants, the xerogels are made of macropores supported by filaments, with each filament being formed of smaller structures. The quantitative impact of the additive on each structural level is assessed. The data are compared with a previous time-resolved SAXS study conducted during the formation of the gels (*J. Phys. Chem. B* 2004, 108, 8983–8991). The results are analyzed in the framework of a double phase separation model.

1. Introduction

The sol–gel process consists of the polymerization of a precursor solution in a solvent until the system gellifies; the liquid phase of the gel is then evacuated during a drying stage and, depending on the drying conditions, a porous solid can eventually be obtained.¹ The mechanism that is most often invoked for explaining the formation of the gel is via an intermediate sol phase, i.e., a colloidal suspension of solid particles. As initially demonstrated by Iler² in the particular case of the polymerization of silicic acid, the condensation of the precursors can lead to the formation of dense colloidal particles. These particles afterward aggregate until their clusters become space filling, at which moment a gel is obtained. This specific type of gels is sometimes referred to as particulate or colloidal.^{1,3} The polymerization of many precursors in various conditions, however, leads to a greater variety of silica gel structures than initially described by Iler. In particular, the use of small-angle X-ray scattering (SAXS) and rheological measurements enabled the existence of polymeric silica gels to be revealed.^{1,3,4} The polymeric silica gels, usually obtained from the polymerization of silicon alkoxides in acidic conditions, bear a strong analogy to some organic gels: they comprise a single phase wherein the weakly branched polymer species are intimately mixed with the solvent.⁵ Incorporating organic molecules into the precursor solutions allows synthesizing materials with an even greater structural diversity.⁶

The formation of the gel's structure can occur via several different mechanisms. When the reacting solution remains homogeneous during the gelling process, the synthesis variables that determine the structure of the gels are those affecting the balance between hydrolysis and condensation of the precursors,

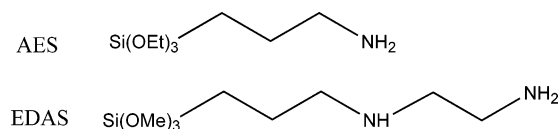
such as the pH, the water content, and the dilution.^{1,2} There is also evidence in some systems that the gelling solution does not remain homogeneous and that phase separation occurs. This phenomenon is frequently encountered for organic polymers,⁷ and it has also been shown for some hybrid materials,⁸ for silica materials synthesized with organic co-reactants,^{9–11} and for some pure silica materials.⁹ In a review of ²⁹Si NMR studies on silica polymerization, Šefčík and McCormick¹² consider phase separation such an important phenomenon that they discuss it on the same footing as hydrolysis and condensation. As polymerization proceeds, the mutual solubility of precursors and solvent decreases, which gives rise to a demixing process. Solvent-rich and polymer-rich phases are formed, with the polymerization possibly continuing in both phases. In this case, the physical phenomena involved in the phase separation process are responsible for much of the morphology of the gels, and the chemical reactions merely play the role of a trigger.

The present study deals with hybrid silica materials synthesized by polymerizing tetraethoxysilane (TEOS) in ethanol in the presence of 3-aminopropyltriethoxysilane (AES) or of 3-(2-aminoethylamino)propyltrimethoxysilane (EDAS) as co-reactants. The use of these particular molecules was previously shown to enable a large porosity to be preserved during the desiccation of the gels, and to obtain highly porous xerogels. In previous works conducted on similar systems, the texture of the xerogels was discussed as resulting from the aggregation of colloidal particles, the size of which depends on the nature and amount of the co-reactants.^{13,14} More recently, however, time-resolved synchrotron SAXS was used to monitor the formation of the nanometric structure of these gels.^{10,15} The collected data hint at a reaction-induced phase separation that is unlikely to lead to particulate structures. Therefore, there seems to be a contradiction between the structures observed on the xerogels and the observation of phase separation during the formation of the gels.

* Corresponding author. Telephone: +32 (0)4 366 47 71. Fax: +32 (0)4 366 35 45. E-mail: Cedric.Gommès@ulg.ac.be.

[†] Université de Liège.

[‡] Katholieke Universiteit Leuven.

SCHEME 1: Organotrialkoxysilane Co-reactants Used in This Work, and Their Abbreviations


The present paper aims at filling the gap between the phase separation process observed during the formation of the gels and the final structure of the xerogels. For that purpose, the texture of these two series of hybrid xerogels is analyzed in detail: nitrogen adsorption measurements, SAXS, and electron microscopy coupled with image analysis are used to characterize the samples. The impact of the co-reactants on the texture of the xerogels at its various relevant length scales is assessed. The textural characteristics of the two families of xerogels are discussed in the light of the previously performed time-resolved SAXS. Finally, the texture development and the role of the co-reactants are discussed in the framework of a double phase separation mechanism.

2. Experimental Section

2.1. Synthesis of the Samples. The synthesis of the samples proceeds as described elsewhere.¹⁰ Gels are prepared from tetraethoxysilane (TEOS), H_2O , ethanol, and NH_3 via a single-step base-catalyzed hydrolysis and condensation, with 3-aminopropyltriethoxysilane (AES) or 3-(2-aminoethylamino)propyltrimethoxysilane (EDAS) as co-reactants. The molecular structure of these molecules is in Scheme 1. To a mixture containing the co-reactant, TEOS, and half the ethanol, a solution of aqueous NH_3 in the remaining ethanol is added under stirring. The stirring is then stopped and the flask is closed. The water solution has a NH_3 content of 0.18 mol/L. The hydrolysis ratio $H = \text{H}_2\text{O}/[\text{TEOS} + (3/4)\text{additive}]$ is 4 for all gels; the 3/4 factor is justified by the fact that both additives contain three hydrolyzable groups, while TEOS contains four of them. A dilution ratio $R = \text{ethanol}/(\text{TEOS} + \text{EDAS}) = 10$ is chosen for all samples. The synthesis is performed at room temperature.

Six AES-based and six EDAS-based samples are studied in this paper, with increasing amounts of co-reactant, whose names and compositions are reported in Table 1. During the reaction, the samples become turbid and eventually gelify; the time for turbidity and the gel time of the samples are reported in the same table. The gel time is determined as the moment when the solution no longer flows when the flask is tilted. The liquid-to-gel transition of the samples is generally abrupt, so the gel times reported in Table 1 are reliable; the transition from transparent to turbid is quite progressive and the reported times must be considered as an indication. At the gel time, the AES gels are white and opaque, and the EDAS gels are milky but translucent, with a slight increase in translucency when more EDAS is used. Sample AT025 never did gelify, even over a period of months, and it resulted in a stable white liquid.

The gels are aged for 7 days at 60 °C. Next, the flasks are opened and put in a drying oven heated at 60 °C where, over a period of a week, the pressure is progressively lowered from atmospheric to about 1000 Pa and the temperature is raised to 150 °C. In their final dry state, the xerogels are all white and opaque, except samples ET10, ET15, and ET20. These latter are yellow, and samples ET15 and ET20 are also translucent.

2.2. Physical Characterization of the Samples. The bulk densities of the xerogels, ρ_b , are measured by mercury pycnometry, i.e., from an independent measurement of the mass

and of volume of a monolithic sample. The skeletal densities of the samples, ρ_s , are measured on a Micromeritics AccuPyc 1330 helium pycnometer. The specific porous volume, is estimated as $V_p = 1/\rho_b - 1/\rho_s$. The porosity is estimated as $\epsilon = 1 - \rho_b/\rho_s$.

Nitrogen adsorption and desorption isotherms are measured at 77 K on a Carlo Erba Sorptomatic 1990 volumetric device, after outgassing the samples overnight at room temperature at a pressure lower than 10^{-4} Pa. The data are analyzed using standard techniques, e.g., ref 16. The porous volume V_{N_2} is estimated from the desorption branch as the amount of nitrogen sorbed at $p/p_0 = 0.98$. The data are also fitted with the BET model, by which the specific surface area S_{BET} and the BET constant C_{BET} are estimated. In describing the texture of the xerogels derived notably from adsorption data, we shall comply with the IUPAC recommendations¹⁷ and call a pore a *micropore* if its width w is less than 2 nm, a *mesopore* if $2 \text{ nm} < w < 50 \text{ nm}$, and a *macropore* if $w > 50 \text{ nm}$.

Small-angle X-ray scattering patterns are collected on a Bruker NanoSTAR apparatus configured with the HI-STAR 2D detector at 107 cm from the sample. The two-dimensional (2D) patterns are corrected for the detector response, for distortions due to the use of a flat detector, and for background. Finally the isotropic patterns are averaged azimuthally and expressed as the scattered intensity as a function of the scattering vector $q = 4\pi/\lambda \sin(\theta/2)$, where λ is the wavelength (1.54 Å), and θ is the scattering angle.

2.3. Microscopy and Image Analysis. Two different methods were used to prepare the samples for observation on a Philips CM100 transmission electron microscope (TEM) operated at 100 kV. In preparation A, the sample was first impregnated with an epoxy resin that polymerized inside its pores; approximately 60 nm thick slices were cut out of the impregnated sample and deposited on the microscopy grid. In preparation B, the sample was crushed in a mortar into a very fine powder, a few milligrams of it was dispersed in ethanol, and the suspension was left a few minutes under ultrasonic agitation. The dispersion was allowed to settle for another few minutes, a drop of the supernatant was deposited on a carbon-coated microscopy grid, and the ethanol was evaporated.

The images obtained from both types of preparation are analyzed using standard techniques of image analysis, using Matlab software and its image processing toolbox. Every image analysis result presented in this paper is an average of measurements performed on about 15 micrographs.

3. Results

3.1. TEM and Image Analysis. Figures 1 and 2 show examples of the micrographs obtained from preparations A and B on the first and last samples of both AES and EDAS series. The two preparations allow the samples to be observed at two different scales: with technique A the large-scale structure of the xerogels is accessible, characterized by lengths of a few hundreds of nanometers, whereas with technique B objects with typical size of a few tens of nanometers are visible.

The large-scale structure of the samples, as visible from A micrographs, consists of large empty spaces separated by elongated structures. In the case of xerogels synthesized with a large amount of EDAS (Figure 2b), no clear feature can be detected, because the structures are smaller than the thickness of the slice. The insets of Figures 1 and 2 are B micrographs, obtained by crushing the samples. The observed fragments of the xerogels correspond to the elongated structures previously described, but they can now be observed without overlap.

TABLE 1: Synthesis of the Samples^a

	co-reactant	R	H	co-reactant/TEOS	$t_{\text{turbidity}}$ (min)	t_{gel} (min)
AT025	AES	10	4	0.025	b	>months
AT05	AES	10	4	0.05	27	95
AT10	AES	10	4	0.10	21	52
AT15	AES	10	4	0.15	19	35
AT25	AES	10	4	0.25	13	21
AT40	AES	10	4	0.40	9	15
ET025	EDAS	10	4	0.025	38	77
ET04	EDAS	10	4	0.04	60	71
ET06	EDAS	10	4	0.06	60	69
ET10	EDAS	10	4	0.10	60	66
ET15	EDAS	10	4	0.15	60	66
ET20	EDAS	10	4	0.20	55	70

^a Co-reactant, nature of the co-reactant; R , dilution molar ratio defined as ethanol/(TEOS + co-reactant); H , hydrolysis molar ratio defined as water/[TEOS + (3/4)co-reactant]; co-reactant/TEOS, molar ratio; $t_{\text{turbidity}}$, elapsed time from the mixing of water with the silica precursors to the moment when the solution loses its transparency; t_{gel} , elapsed time from the mixing of water with the silica precursors to the moment when the solution no longer flows. ^b Not measured.

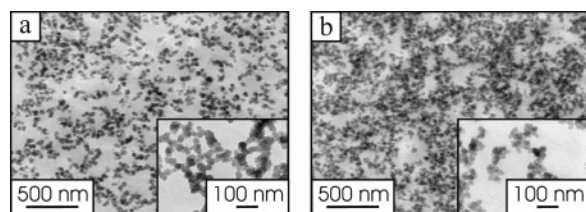


Figure 1. Typical TEM micrographs of AES gels AT05 (a) and AT40 (b). The main images are typical of the impregnated samples (preparation A), and the insets are typical of the crushed samples (preparation B).

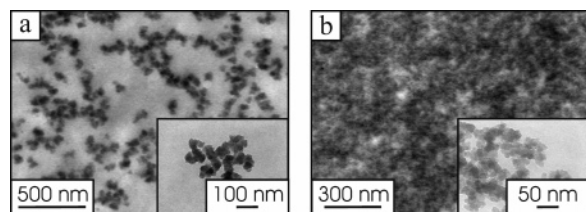


Figure 2. Typical TEM micrographs of EDAS gels ET025 (a) and ET20 (b). The main images are typical of the impregnated samples (preparation A), and the insets are typical of the crushed samples (preparation B).

Because of local bulges in these structures (e.g., inset of Figure 1a), they are sometimes referred to as “strings of pearls” in the sol–gel literature, e.g., refs 1 and 2. For the present samples, however, the pearls are generally poorly defined, and we shall refer to these structures as *filaments*. On most type B micrographs, the filaments seem to have a substructure. This is particularly clear for the sample synthesized with the lowest amount of AES that resulted in a white liquid that did never gelify. The filament structure is also present in this sample (Figure 3a), and smaller objects are also visible (Figure 3b) that seem to be their building blocks (Figure 3c). Although we have no general evidence that these structures are particulate, we shall refer to them as *particles*. On all other samples particles are not isolated, and they are only visible as small globular objects that protrude out of the filaments as in Figure 3c. To make these observations more quantitative, the characteristic sizes of the pores, filaments, and particles were measured using image analysis.

The regions between neighboring filaments are the pores of the samples. Their width, L_{pore} , was estimated from type A micrographs. Since these are projections of 60 nm thick slices, they can reliably be used to measure objects larger than that size. Because the shape of the pore space is complex, L_{pore} was estimated using an opening granulometry.^{18,19} The principle of

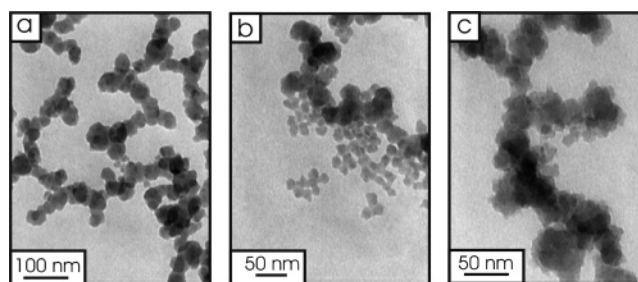


Figure 3. Example of TEM micrographs obtained from sample AT025, on which (a) the filaments, (b) the particles, and (c) the particles within the filaments are visible.

this method is reviewed in the Appendix, and it basically consists of assigning a size L to any region of the images that can contain a disk of diameter L . This idea is closely related to the more familiar concept of chord length, often used to measure objects with a complex shape.¹⁹ An additional advantage of the method is that it does not require any user intervention and that it is therefore totally objective. The values of L_{pore} reported in Table 2 show that the size of the pores is almost the same for all AES samples, and that the pores become much smaller when more EDAS is used. When L_{pore} is smaller than about 60 nm, the size of the pores might be underestimated, because of the projection effects involved.

Since the width of the filaments L_F is smaller than 60 nm, they might overlap in the slices used for obtaining type A micrographs. Preparation B was therefore used, by which the samples were crushed and only fragments were observed. To avoid user subjectivity, an opening granulometry was also used to estimate L_F . It should be stressed that the smallest objects visible in the cuts are comparable in size to L_F , which means that the crushing of the samples did not modify the width of the filaments. The values of L_F reported in Table 2 show that the width of the filaments slightly decreases when more AES is used. This effect is much more marked for EDAS. There is an abrupt increase of L_F from ET15 to ET20. This jump probably reflects a different structure of sample ET20 (see insets of Figure 2), and the value of L_F should not be interpreted as the width of the filaments for this sample.

The measurement of the diameter of the particles, L_{part} , is more problematic as the filaments could not be physically decomposed into particles, which would have enabled their unambiguous observation. The same micrographs as for the filaments were therefore used. As the particles overlap everywhere, no user-free method could be used. However, globular structures are visible on the edges of the filaments and they

TABLE 2: Characteristic Lengths of the Samples, Obtained from Various Characterization Techniques^a

	L_{pore} (nm)	L_F (nm)	L_{part} (nm)	l_s (nm)	l_p (nm)	L_{SAXS} (nm)	L'_{SAXS} (nm)
AT05	87	37	12 ± 1	9	46	>40	c
AT10	77	34	13 ± 2	14	64	31	c
AT15	76	31	13 ± 2	15	66	31	c
AT25	71	31	15 ± 2	16	68	b	b
AT40	64	29	13 ± 2	19	69	31	c
ET025	240	45	16 ± 2	12	69	>40	16
ET04	135	33	14 ± 2	10	56	c	12
ET06	57	27	11 ± 2	9	46	c	c
ET10	28	15	7.6 ± 1	8	36	16	c
ET15	23	13	7.0 ± 1	8	32	12	c
ET20	9	(26)	11 ± 2	6	18	6	c

^a L_{pore} , size of the pores obtained from the opening granulometry of type A micrographs; L_F , width of the filaments obtained from the opening granulometry of type B micrographs; L_{part} , size of the particles measured manually on type B micrographs; l_s and l_p , solid and pore chord lengths; L_{SAXS} and L'_{SAXS} , first and second characteristic sizes estimated by SAXS. ^b Data not available. ^c Not measurable.

TABLE 3: Textural Characteristics of the Samples^a

	ρ_b (g/cm ³)	ρ_s (g/cm ³)	V_p (cm ³ /g)	ϵ	V_{N_2} (cm ³ /g)	C_{BET}	S_{BET} (m ² /g)
AT05	0.39	2.26	2.15	0.83	1.50	142	187
AT10	0.38	2.08	2.17	0.82	1.40	89	136
AT15	0.38	2.02	2.12	0.81	0.85	79	129
AT25	0.38	1.96	2.11	0.81	1.53	36	124
AT40	0.40	1.88	1.94	0.78	1.02	53	113
ET025	0.30	2.65	2.84	0.85	0.53	320	165
ET04	0.32	2.13	2.62	0.85	0.67	124	179
ET06	0.34	2.10	2.49	0.84	0.90	94	215
ET10	0.37	2.04	2.18	0.82	1.34	72	243
ET15	0.39	1.97	2.07	0.80	1.53	75	256
ET20	0.50	1.91	1.49	0.74	1.52	54	327

^a ρ_b , bulk density; ρ_s , skeletal density; V_p , porous volume; ϵ , porosity; V_{N_2} , amount of nitrogen adsorbed at $p/p_0 = 0.98$; C_{BET} , BET constant; S_{BET} , BET specific surface area.

were measured manually. The values of L_{part} reported in Table 2 are the average and standard deviation of particle size measured on 15 type B micrographs for each sample. The particles were only considered when they were clearly visible, which led to approximately 20 particle measurements for each sample. The data in Table 2 show that the size of the particles is unchanged when more AES is used and that it decreases markedly when more EDAS is used. At this stage, it is however admitted that the reliability of L_{part} rests mainly on how the values will compare with the other characterization data, which issue is analyzed in the Discussion.

3.2. Pycnometry and Nitrogen Adsorption. The bulk and skeletal densities, ρ_b and ρ_s , obtained from mercury and helium pycnometry, are reported in Table 3. For both AES and EDAS samples, increasing the amount of co-reactant results in a lowering of the skeletal density. For the AES xerogels no marked evolution is observed for the bulk density, while a marked increase in ρ_b is observed when the amount of EDAS is increased.

Figure 4 reports the nitrogen adsorption–desorption isotherms measured on the xerogels, and the corresponding textural characteristics are in Table 3. The isotherms of all the AES samples (Figure 4a) are of type II^{16,17} with a very narrow hysteresis at high pressure, as is generally observed for nonporous or macroporous solids. This is also the case for the samples synthesized with a small amount of EDAS (ET025 to ET06). On the contrary, for larger amounts of EDAS (ET10 to ET20), the isotherms progressively become of type IV, which is typical of mesoporous solids wherein capillary condensation occurs.^{16,17} The porous volume V_{N_2} exhibits no clear trend when the amount of AES is increased (AT05 to AT40), whereas for EDAS xerogels it clearly increases when more additive is used (ET025 to ET20). For all samples V_{N_2} is much lower than V_p ,

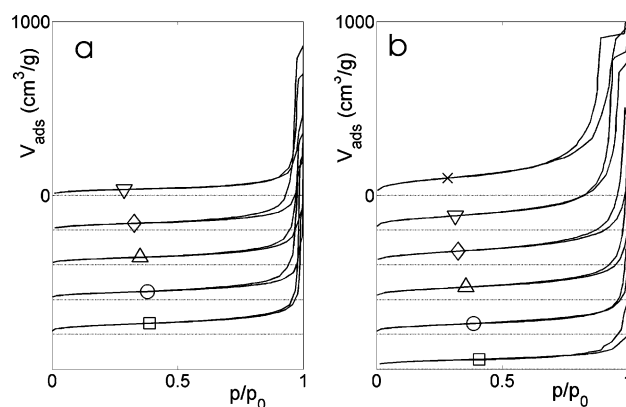


Figure 4. Nitrogen adsorption and desorption isotherms measured (a) on AES xerogels AT05 (□), AT10 (○), AT15 (△), AT25 (◇), and AT40 (▽); and (b) on EDAS xerogels ET025 (□), ET04 (○), ET06 (△), ET10 (◇), ET15 (▽), and ET20 (×). The isotherms are arbitrarily shifted vertically.

except for those synthesized with a large amount of EDAS (ET15 and ET20).

The specific surface S_{BET} undergoes a 40% decrease when the amount of AES is increased (from AT05 to AT40), but it almost doubles when the amount of EDAS is increased (from ET025 to ET20). The BET constant, C_{BET} , is representative of the energy of interaction between the nitrogen molecule and the surface of the xerogels, and it can serve as a measure of the polarity of the adsorbent surface. It decreases when the amount of any co-reactant increases (Table 3).

The general concept of chord length allows relating the specific surface of a solid to the characteristic size of its skeleton or pores, independently of its geometry.^{20,21} Let a two phase (A–B) solid be penetrated by a test line. The chord length of

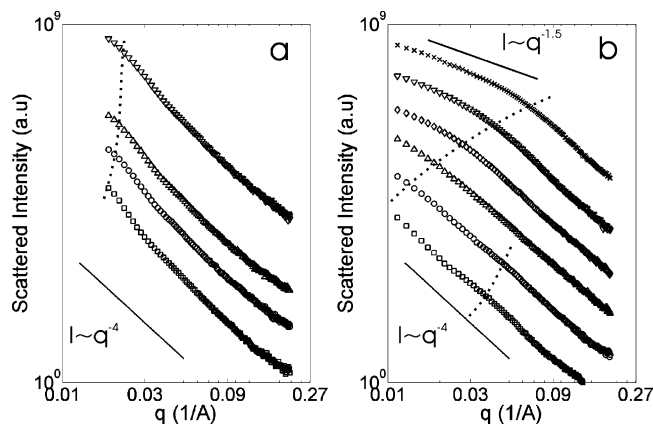


Figure 5. Small-angle X-ray scattering patterns measured (a) on AES gels AT05 (\square), AT10 (\circ), AT15 (Δ), and AT40 (∇); and (b) on EDAS gels ET025 (\square), ET04 (\circ), ET06 (Δ), ET10 (\diamond), ET15 (∇), and ET20 (\times). The dotted lines highlight the evolution of the characteristic lengths upon increasing the amount of additive.

phase A, l_A , is defined as the average length of the intersections of the test line with phase A. Under general assumptions, it can be shown that the chord length is related to the specific volume, V_A , and specific area of the interface, S_{AB} , through the relation $l_A = 4V_A/S_{AB}$.²⁰ This relation can be used to estimate the pore chord l_p and solid chord l_s of a porous solid as

$$l_p = \frac{4V_p}{S_{BET}} \quad \text{and} \quad l_s = \frac{4}{\rho_s S_{BET}} \quad (1)$$

where V_p is the porous volume estimated by pycnometry, and the specific volume of the skeleton is replaced by $1/\rho_s$ in the second relation. The pore and solid chord lengths, l_p and l_s , are reported in Table 2 together with the other characteristic lengths. For all analyzed samples, l_p is larger than l_s , as expected for low-density materials. For AES samples, both l_p and l_s increase when the amount of co-reactant is increased. For EDAS samples, both l_p and l_s decrease.

3.3. Small-Angle X-ray Scattering. The SAXS patterns measured on the samples are displayed in Figure 5. The patterns of AES xerogels (Figure 5a) follow a power law with an exponent slightly larger than 4 over a limited range of scattering vector q . The existence of a Porod region, with exponent 4, is typical of the scattering by objects having a smooth surface.²² A deviation from the power law is observed at low q , and the value of q at which the deviation is observed is inversely related to the size of the scattering objects. Practically, the characteristic size of the scattering objects was determined from a Kratky–Porod plot of the SAXS data (not shown),²² as $L_{SAXS} = 2\pi/q_{max}$, where q_{max} is the position of the maximum of Iq^4 . This length is reported in Table 2. For AT05, Iq^4 continuously decreases with increasing q , which means that L_{SAXS} is larger than the limit of the SAXS (about 40 nm for the configuration used). The dotted line in Figure 5a is a guide for the eye, and it passes approximately through the estimated values of L_{SAXS} .

The SAXS patterns of the EDAS xerogels are more complex (Figure 5b). For the sample synthesized with the largest amount of EDAS (ET20), the SAXS exhibits a Porod scattering at high angles, and a power law scattering with an exponent slightly greater than 1 at lower angles. In the present context, such a pattern can typically be interpreted as the scattering from filaments, with a diameter corresponding to the cutoff between the two observed power laws, and whose length is too large for the measured q range.²² Decreasing the amount of EDAS (from ET20 to ET06), the shape of the scattering patterns

remains unchanged, but the cutoff shifts toward smaller angles, which means that the diameter of the filaments becomes larger. For the sample with the smallest amount of EDAS (ET025), the diameter becomes larger than about 40 nm and it leaves the measured q range. The diameters of the filaments are also called L_{SAXS} and are reported in Table 2. These were calculated as previously from a Kratky–Porod plot. For ET04 and ET06, the q^4 trend does not extend over the entire q range but Iq^4 exhibits no maximum, and L_{SAXS} could not be estimated. For samples ET04 and ET025, a slight hump is present in the middle of the Porod region (see Figure 5b). The very presence of a hump suggests that the interior of the filaments is not uniform, but that it has itself a structure. The length scale of these substructures, corresponding to the q position of the hump through the approximate relation $L'_{SAXS} = 2\pi/q$, is also reported in Table 2.

4. Discussion

4.1. Local and Global Evidence for the Hierarchical Structure of the Xerogels. Electron microscopy shows that the structure of AES and EDAS xerogels is hierarchical. It is formed of a macroporous spongelike structure, supported by filaments, with each filament being made of smaller structures that we called particles. Evidence of this structure needs to be found in the global macroscopic characterization data. For that purpose, the characteristic length of each identified structural level (macropores, filaments, and particles) was estimated from the micrographs.

The large-scale structure of the samples is supported by macroscopic evidence. First, the volume of nitrogen sorbed near the saturation, V_{N_2} , is a fraction of the porous volume V_p estimated from pycnometry, which points at the existence of macropores.^{16,17} Furthermore, an analysis of the adsorption data of ET025 and ET04²⁵ shows that the adsorbent surface is convex, with a radius of curvature that compares well with the width of the filaments. In the present study, the width of the filaments measured by TEM, L_F , compares well with L_{SAXS} (Table 2), which suggests that the structures observed by TEM are representative of the macroscopic samples.

An important issue is the existence of a substructure within the filaments, which we call particles. For the sample with the lowest amount of AES, which did not lead to a gel, the existence of globular objects within the filaments is evident from TEM (Figure 3). For the samples with a small amount of EDAS, it is also seen from SAXS that structures with a size smaller than the filaments do exist (Figure 5b). As for ET025 and ET04, L_{SAXS} compares well with the size of the particles measured manually on the edges of the filaments, L_{part} ; the particles can reasonably be thought to exist in these samples as well.

Samples with larger amounts of co-reactant lack macroscopic evidence of particles. For AES samples, it can, however, be noted that S_{BET} decreases when more AES is used, while the width of the filaments L_F remains almost unchanged, and even slightly decreases (Tables 2 and 3). It must therefore be admitted that there is an inner structure within the filaments, whose developed surface area becomes lower when more AES is used. A similar conclusion can be reached for EDAS samples. However, because all the structures become smaller when more EDAS is used, it is impossible to argue on the basis of S_{BET} alone, and chord lengths must be considered. For ET025, the solid chord length is much smaller than the width of the filaments, but it compares well with L_{part} (Table 2). This means that the filaments alone cannot explain the observed value of S_{BET} , and that it can only be obtained with objects of the same

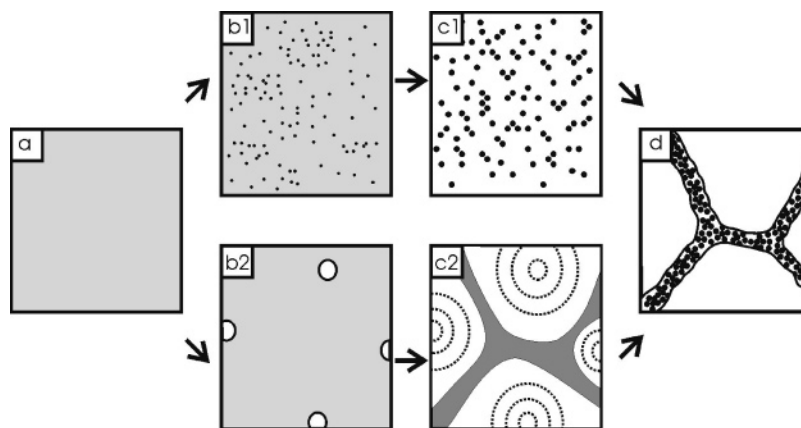


Figure 6. Possible bottom-up (upper path) and top-down (lower path) mechanisms to explain the transition from a homogeneous polymerizing solution (a) to a spongelike filamentary structure with filaments made of particles (d). Bottom-up mechanism: (b1, c1) nucleation and growth of silica particles; (c1, d) aggregation of the particles to create the filamentary structure. Top-down mechanism: (b2, c2) nucleation and growth of solvent vacuoles; (c2, d) secondary phase separation by which the particles are created within the filaments.

size as the particles. The same conclusion can be reached from the pore chord length l_p , which is significantly smaller than L_{pore} for ET025. This means that pores smaller than those visible on type A micrographs must be present in that sample. On the contrary, for the samples with large amounts of EDAS, l_p compares well with L_{pore} , although image analysis probably underestimates the pore size for these samples (see section 3.1).

In summary, the macropore–filament–particle hierarchical structure of the xerogels derived from TEM is in agreement with the macroscopic characterization data. The size of these structures is almost independent of the amount of AES, but it decreases markedly when more EDAS is used. Finally, for large amounts of any co-reactant, the filaments are bulky and they progressively decompose into particles for lower amounts of co-reactant.

4.2. Possible Mechanisms for the Structuring of the Gels.

The fact that each structural level of the xerogels has a well-defined length scale suggests that the whole structure results from the *succession* of different physicochemical events, rather than from their simultaneous occurrence. Generally, the succession of events leading to the final material can be bottom-up (BU) or top-down (TD), e.g., ref 26. In the former case, the smallest structures are obtained first and the larger structures are built using the smaller ones as building blocks. In the latter case, the largest structures are first obtained and the smaller objects result from a process that occurs within these larger structures.

The aggregation model is typically bottom-up.^{1,2} Using this model for EDAS and AES gels, one would have to admit that the initially homogeneous reacting solution leads first to the formation of particles, and then to their aggregation into filaments until a percolating network is formed at the gel point (upper path of Figure 6). Several chemical mechanisms could explain the formation of monodisperse particles, e.g., ref 27. It would, however, be unclear why their aggregation would lead to anisotropic structures such as filaments. One would also expect fractal-like structures with no characteristic size,^{1,28} whereas the structures of EDAS and of AES gels have well-defined characteristic lengths. Moreover, in a BU approach, the formation of the large-scale percolating network is the last event. It has been observed for both AES and EDAS gels that the time for turbidity is significantly lower than the gel time (Table 1). Turbidity is associated with the formation of structures whose size is comparable to the visible light wavelength. This means that the largest structures of the gels, corresponding to the largest

pores of the final xerogels, are formed well before the gel point. Furthermore, time-resolved SAXS¹⁰ shows that the nanometric structures of EDAS gels, i.e., the particles and the filaments, are not necessarily formed when gelation occurs. Therefore, a BU model alone can hardly explain the formation of the structure of the studied xerogels.

Top-down processes are often encountered during the structuring of organic polymer blends, e.g., ref 7. When the mutual solubility of two polymers A and B lowers, resulting, e.g., from a curing reaction, a phase separation can occur that leads to the creation of an A-rich phase and a B-rich phase that are thermodynamically stable for the given state of curing. As the reactions continue in each phase, these can later become unstable again and an additional phase separation can occur, leading to a further structuring of the A-rich and B-rich phases. This process leads to a hierarchical structure containing as many structural levels as successive phase separations, and as many as three successive phase separations can be obtained, e.g., ref 29.

The succession of possible events involved in a TD process for the formation of the studied gels is illustrated by the lower path of Figure 6. As the hydrolysis and condensation of the precursors go on, their solubility in the solvent decreases, which triggers the phase separation.^{9,12} In the present case of high molecular weight molecules, it is likely that a viscoelastic phase separation is at work.³⁰ This scenario is universally encountered whenever the demixing species have different rheological properties, in which case regions of the least viscous phase nucleate and grow. According to these arguments, we shall assume that the phase separation in AES and EDAS gels occurs first through the appearance and growth of solvent vacuoles (Figure 6b2). Once the nucleated vacuoles have grown and touch each other, the silica is concentrated in a phase that bears the morphology of a sparse columnar network (Figure 6c2). In organic polymer solutions, similar structures are known to result from a competition between gelation and phase separation.^{31,32} Since the reactions continue in the silica-rich phase, a secondary phase separation can occur, by which the already created filaments decompose into smaller regions, which we called particles (Figure 6d).

This TD scenario would explain the various structural levels of AES and EDAS xerogels. Moreover, the secondary phase separation is directly supported by time-resolved synchrotron SAXS.^{10,15} The length scales analyzed in these studies encompass the size of the structures that we call *particles* in the present

paper. The main features of these measurements were as follows: first, the appearance and growth of a maximum in the SAXS patterns; second, its shift toward smaller angles; and in the meantime a significant increase of the intensity scattered at very low angles. These features were interpreted as a reaction-induced spinodal phase separation³³ in the 3–50 nm range, together with the appearance of larger structures. SAXS also shows that the evolution of the nanometer structure can continue long after the gel point. The chronology of the events leading to the formation of the samples is the following (see also Table 1). (i) The reacting solution becomes turbid, which means that structures comparable in size to the visible light wavelength have appeared. In the previous SAXS studies, this corresponds to the appearance of a scattered intensity at very low angles. We now call this process the primary phase separation, and it leads to the macropores and filaments. (ii) Gelation occurs as a consequence of the condensation reactions continuing in the silica-rich phase. (iii) The formation of the particles within the filaments occurs in the meantime, and it continues after the gel point. It is this secondary phase separation that was previously followed by SAXS.^{10,15}

A marked effect of AES is to speed up the gel formation, visible by its impact on the gel time (Table 1). In alkaline conditions, however, organically substituted trialkoxysilanes are known to be less reactive toward hydrolysis and condensation than tetraalkoxysilanes.^{1,6} The accelerating effect of AES could result from the presence of the amine that would act as an “internal” catalyst of the molecule,²⁴ but the very occurrence of phase separation suggests that physical effects can play an important role as well.¹² For instance, the AES molecule (Scheme 1) could possess an amphiphilic character with a silicon alkoxide head and an organic moiety having different affinities for the two phases. AES could therefore speed up the phase separation, by lowering the surface tension between silica and ethanol phases. The AES molecules would act as surfactants and would be statistically localized at the silica–ethanol interface. This could be the origin of the lowering of C_{BET} when more co-reactant is used (Table 3). Since C_{BET} is a measure of the polarity of the adsorbent surface, this trend suggests that the weakly polarized propyl groups cover the adsorbent surface, as also reported for similar systems.^{23,24}

The role of EDAS is possibly 2-fold. Owing to its structure (Scheme 1), it should have an amphiphilic character and favor the phase separation, but it is also far more reactive than TEOS and its role cannot be only physical. For instance, the rate of hydrolysis of AES and of EDAS under the same conditions is 0.38 h⁻¹ and 340 h⁻¹, respectively.³⁴ EDAS can therefore only play the role of a surfactant for a very limited period: once it has hydrolyzed and possibly condensed with other molecules, its role must change. The polymerization of TEOS is an autoaccelerating process because highly condensed species are more prone to hydrolyze and condense than monomeric TEOS.^{1,2,12} Therefore, a small amount of more reactive EDAS might seed the polymerization and accelerate the whole reaction. With more EDAS, the degree of reticulation can grow rapidly enough to slow the primary phase separation and possibly stop it before it is complete. This would explain the effect of EDAS on the size of the largest pores. Moreover, the length scale at which the secondary phase separation occurs results from a compromise between the lyophobicity of the species, which favors the formation of large domains, and the reticulation that favors a short-scale phase separation, e.g., ref 11. Therefore, increasing the reticulation of the silica network, for instance

by increasing the amount of EDAS, should naturally lead to smaller structures.

5. Conclusions

The present study fills the gap that previously existed between the texture of EDAS and AES xerogels^{13,14} and the in situ monitoring of the formation of the gels by synchrotron SAXS.^{10,15} For that purpose, a set of independent characterization techniques was applied to investigate the texture of the two series of xerogels. The global structures of both AES and EDAS xerogels comprise several structural levels with well-defined length scales: the largest structure is that of the macropores; these are supported by elongated filaments, and each filament is made of smaller structures. Increasing the amount of AES accelerates the gel formation but leaves its final structure almost unchanged. Increasing the amount of EDAS does not significantly affect the gel time, but it shifts the final structure toward smaller sizes.

The hierarchy of structural levels and the fact that the largest structures are formed before the smallest ones hint at multiple phase separation. A primary phase separation is responsible for the formation of the largest pores and filaments, and a secondary phase separation creates the smallest structures within the filaments. These two processes were already observed in the previously published time-resolved SAXS study, but the present textural analysis gives all their import to these previous results. Finally, the different effect of the two co-reactants can also find a reasonable explanation within the double phase separation model.

Acknowledgment. C.J.G. is grateful to the FNRS (National Fund for Scientific Research, Belgium) for a Ph.D. Research Fellow position. B.G. is postdoctoral fellow of the Fund for Scientific Research Flanders (FWO-Vlaanderen). The authors, M.B. in particular, are grateful to Em. Prof. H. Reynaers (KULeuven) and the FWO-Vlaanderen for financial support also with respect to the NanoSTAR (G0222.00). This work was supported by the Fonds de Bay, the Fonds de la Recherche Fondamentale et Collective, the Ministère de la Communauté Française de Belgique (ARC 00/05-265), and the Ministère de la Région Wallonne.

Appendix: Opening Granulometry

Opening granulometry is a general tool developed in the framework of mathematical morphology to analyze both binary and gray level images. In this Appendix, we shall only review in an intuitive way its principle, and the interested reader should consult ref 35 for a thorough mathematical presentation.

An image is an intensity function of two spatial variables $I(x,y)$. Any morphological filter uses a geometric object called a structuring element (SE) with which the image is compared. Typically, for a one-dimensional (1D) image the SEs can be segments of various lengths; for a 2D image they can be disks of various diameters, squares, etc. To understand how an opening filter modifies an image, it is convenient to visualize it as a topographic surface, where the gray level is converted to an altitude.

The case of a 1D image, $I(x)$, scanned with a segment as an SE is illustrated in Figure 7a. For each position of the segment, it is pushed upward from beneath until it touches the $I(x)$ curve. The opening of $I(x)$ by the segment is defined as the upper envelope of all the positions reached by the segment. If the size of SE is smaller than the features of $I(x)$, it can be pushed everywhere very close to the curve and the opening has almost

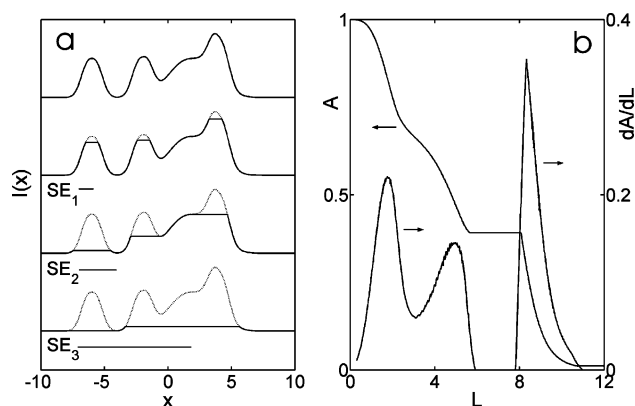


Figure 7. Principle of opening granulometry. (a) Applying an opening filter to a given function $I(x)$, is equivalent to trying to push a structuring element (SE) into the details of it from beneath. The characteristic sizes of $I(x)$ are obtained by considering the remaining area, A , under the curves of $I(x)$ after opening as a function of the size L of SE. The characteristic sizes are the maxima of the derivatives dA/dL .

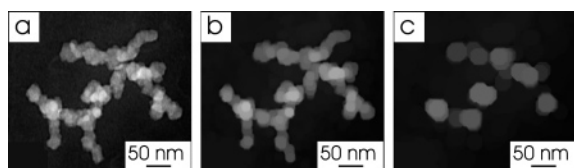


Figure 8. (a) Example of a type B micrograph (sample AT10), inverted to make the silica appear bright, and the same image after opening with a disk of diameter $L = 16$ nm (b), and $L = 32$ nm (c).

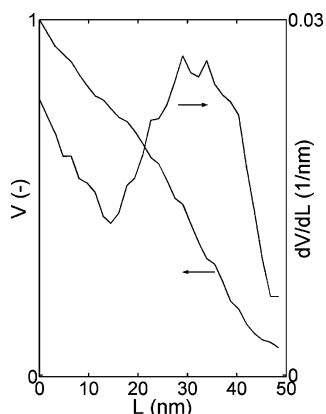


Figure 9. Cumulative opening granulometry curve, $V(L)$, obtained from the image of Figure 8a, and its derivative $-dV/dL$.

no effect on $I(x)$. On the contrary, if the size of SE is larger than, say, the width of the humps in $I(x)$, these will be removed by the opening, but the larger features of $I(x)$ will still be preserved. In Figure 7a, the opening of a given function by segments of increasing lengths is considered. SE_1 is small enough to enter the humps of $I(x)$, SE_2 is larger than the humps, but it can still enter the larger features resulting from the superposition of two humps (at $x \sim 5$), and SE_3 can only enter the objects resulting from the superposition of three humps. The total area under the curve of $I(x)$ after opening with a segment of length L , $A(L)$, is a decreasing function of L . If only features of size L_0 were present in $I(x)$, then $A(L)$ would decrease markedly only near $L = L_0$, and the derivative $-dA/dL$ would exhibit a peak at that position. The granulometry curves of Figure 7a, $A(L)$ and $-dA/dL$, are plotted in Figure 7b. The dA/dL curve exhibits three peaks at $L = 2$, at $L = 5$, and at $L = 8$. These values correspond to the three characteristic lengths of $I(x)$, resulting (i) from the individual humps, (ii) from the

superposition of two humps, and (iii) from the superposition of three humps.

The same procedure can be applied to analyze a 2D gray level image, using a 2D structuring element. This is illustrated in Figure 8, where a given image is opened with disks of increasing diameter. The original image (Figure 8a) is a type B micrograph that has been inverted to make the silica appear bright. The volume of this image, V , is defined as the volume under its topographic equivalent surface, equivalent to the mean gray level of all the pixels in the image. Opening the image with a disk of 16 nm diameter only results in a smoothing of the silica skeleton (Figure 8b), and V does not decrease significantly. On the contrary, a significant fraction of the silica skeleton is removed by an opening with a disk of 32 nm diameter (Figure 8c). Figure 9 plots the volume $V(L)$ of the image of Figure 8a after opening with disks of increasing diameters L . The derivative $-dV/dL$ exhibits a maximum at $L \sim 30$ nm, corresponding to characteristic size of the silica skeleton.

References and Notes

- (1) Brinker, C. J.; Scherer, G. W. *Sol-Gel Science: the Physics and Chemistry of Sol-Gel Processing*; Academic Press: San Diego, 1990.
- (2) Iler, R. K. *The Chemistry of Silica: Solubility, Polymerization, Colloid and Surface Properties, and Biochemistry*; Wiley: New York, 1979.
- (3) Brinker, C. J.; Scherer, G. W. *J. Non-Cryst. Solids* **1985**, *70*, 301–322.
- (4) Schaefer, D. W.; Keefer, K. D. *Phys. Rev. Lett.* **1984**, *53*, 1383–1386.
- (5) Tanaka, T. *Sci. Am.* **1981**, 124–138.
- (6) Avnir, D.; Levy, D.; Schubert, U.; Wojcik, A. B. In *The Chemistry of Organic Silicon Compounds*; Rappoport, Z., Apeloig, Y., Eds.; Wiley: Chichester, 1998; Vol. 2, p 2371.
- (7) Olabisi, O.; Robeson, L. M.; Shaw, M. T. *Polymer-Polymer Miscibility*; Academic Press: New York, 1979.
- (8) Ulibarri, T. A.; Beaucage, G.; Schaefer, D.; Olivier, B. J. Assink, R. A. *Mater. Res. Soc. Symp. Proc.* **1992**, *274*, 85–90.
- (9) Nakanishi, K. *J. Porous Mater.* **1997**, *4*, 67–112.
- (10) Gommes, C. J.; Blacher, S.; Goderis, B.; Pirard, R.; Heinrichs, B.; Alié, C.; Pirard, J.-P. *J. Phys. Chem. B* **2004**, *108*, 8983–8991.
- (11) Schaefer, D. W.; Beaucage, G.; Loy, D. A.; Shea, K. J.; Lin, J. S. *Chem. Mater.* **2004**, *16*, 1402–1410.
- (12) Šefčík, J.; McCormick, A. V. *Catal. Today* **1997**, *35*, 205–223.
- (13) Alié, C.; Pirard, R.; Lecloux, A. J.; Pirard, J.-P. *J. Non-Cryst. Solids* **1999**, *246*, 216–228.
- (14) Alié, C.; Ferauche, F.; Pirard, R.; Lecloux, A. J.; Pirard, J.-P. *J. Non-Cryst. Solids* **2001**, *289*, 88–96.
- (15) Gommes, C. J.; Blacher, S.; Goderis, B.; Pirard, J.-P. *Nucl. Instrum. Mater. Sci. B* **2005**, *238*, 141–145.
- (16) Lecloux, A. J. In *Catalysis: Science and Technology*; Anderson, J. R., Boudart, M., Eds.; Springer: Berlin, 1981; Vol. 2, pp 171–230.
- (17) Rouquerol, J.; Avnir, D.; Fairbridge, C. W.; Everett, D. H.; Haynes, J. H.; Pernicone, N.; Ramsay, J. D. F.; Sing, K. S. W.; Unger, K. K. *Pure Appl. Chem.* **1994**, *66*, 1739.
- (18) Soille, P. *Morphological Image Analysis: principles and applications*; Springer: Berlin, 1999.
- (19) Ohser, J.; Mücklich, F. *Statistical Analysis of Microstructures in Materials Science*; Wiley: Chichester, 2000.
- (20) Russ, J. C.; Dehoff, R. T. *Practical Stereology*, 2nd ed.; Plenum Press: New York, 1999.
- (21) Schaefer, D. W.; Beaucage, G.; Loy, D. A.; Shea, K. J.; Lin, J. S. *Chem. Mater.* **2004**, *16*, 1402–1410.
- (22) Glatter, O.; Kratky, O. *Small-Angle X-ray Scattering*; Academic Press: New York, 1982.
- (23) Hüsing, N.; Schubert, U.; Misof, K.; Fratzl, P. *Chem. Mater.* **1998**, *10*, 3024–3032.
- (24) Hüsing, N.; Schubert, U.; Mezei, R.; Fratzl, P.; Riegel, B.; Kiefer, W.; Kohler, D.; Mader, W. *Chem. Mater.* **1999**, *11*, 421–457.
- (25) Gommes, C. J.; Blacher, S.; Pirard, J.-P. *Langmuir* **2005**, *21*, 1703–1705.
- (26) *Nanoscience and Nanotechnologies: Opportunities and Uncertainties*; The Royal Society & The Royal Academy of Engineering: London, 2004.
- (27) Lee, K.; Look, J.-L.; Harris, M. T.; McCormick, A. V. *J. Colloid Interface Sci.* **1997**, *194*, 78–88.
- (28) Viscek, T. *Fractal Growth Phenomena*, 2nd ed.; World Scientific: Singapore, 1992.

- (29) Vanden Poel, G.; Goossens, S.; Goderis, B.; Groeninckx, G. *Polymer* **2005**, *46*, 10758–10771.
- (30) Tanaka, H. *Phys. Rev. Lett.* **1996**, *76*, 787–790.
- (31) Aubert, J. H. *Macromolecules* **1988**, *21*, 3468–3473.
- (32) Jackson, C. L.; Shaw, M. T. *Polymer* **1990**, *31*, 1070–1084.
- (33) Bates, F. S.; Wiltzius, P. *J. Chem Phys.* **1989**, *91*, 3258–3274.
- (34) Brand, M.; Frings, A.; Jenkner, P.; Lehnert, R.; Metternich, H. J.; Monkiewicz, J.; Schram, J. *Z. Naturforsch.* **1999**, *54b*, 155–164.
- (35) Serra, J. *Image Analysis and Mathematical Morphology*; Academic Press: London, 1982; Vol. 1.